Covalency competition triggers Fe-Co synergistic catalysis for boosted Fenton-like reactions

Wenqian Li [a], Shuangqing Xia [a], Zhenyi Wang [a], Bin Zhang [a], Boda Li [a], Lijuan Zhang [b,c], Kun Qian [d], Jun Ma [a], Xu He [a,*]

[a] *State Key Laboratory of Urban Water Resource and Environment, School of Environment, Harbin Institute of Technology, Harbin 150090, China*
[b] *Key Laboratory of Interfacial Physics and Technology, Chinese Academy of Sciences, Shanghai 201800, China*
[c] *Shanghai Synchrotron Radiation Facility, Shanghai Institute of Applied Physics, Chinese Academy of Sciences, Shanghai 201204, China*
[d] *State Key Laboratory of Pollution Control and Resources Reuse, College of Environmental Science and Engineering, Tongji University, Shanghai 200092, China*

ARTICLE INFO

ABSTRACT

Fe-Co based oxides demonstrate excellent Fenton-like catalytic activity, but the intrinsic mechanism of Fe-Co synergy remains elusive. Here, we uncover the influence of covalency competition between Fe and Co on catalytic behaviors in peroxymonosulfate (PMS) activation. Theoretical and experimental analysis reveals that higher electron delocalization of octahedral Co (Co_{Oh})-O unit and lower electron delocalization of Fe_{Oh}-O unit boost electron transfer between Co and O species and transformation of $SO_5^{\bullet-}$ towards surface-bounded and free $SO_4^{\bullet-}$ instead of $^1O_2$. With favorable covalency competition, electron transfer capability, active oxidizing species, $(Co_{0.8}Fe_{0.2})_{Oh}$-O unit exhibits superior activity with rate constant of 0.27 min^{-1}, 254.7, 37.5 and 2.2 times of that in PMS, Fe_{Oh}-O unit/PMS and Co_{Oh}-O unit/PMS systems, respectively, outperforming all the reported Fe-Co based oxides in removal of refractory pollutants. The improved insights into the origin of Fe-Co synergy advance the rational development of highly efficient catalytic oxidation systems for water decontamination.

1. Introduction

The pursuit of clean water drives innovation in advanced water treatment technologies. Peroxymonosulfate (PMS)-based advanced oxidation has been regarded as a promising strategy to degrade recalcitrant organic contaminants, owing to adaptability to a wide pH range and easy availability of various oxidizing reactive species [1]. Transition metal (TM) oxides are among the most studied PMS activators, benefiting from their earth-abundance, cost-effectiveness, excellent redox properties and catalytic performance [2]. Since TM center is recognized as the catalytic site, its redox cycling can profoundly influence the catalytic activity [3,4]. For example, Mn_2O_3 acts as an electron shuttle between PMS and pollutant, with dual roles in catalytical decomposition of PMS by Mn^{3+} and direct oxidation of pollutants by Mn^{4+}, to sustain Mn^{3+}/Mn^{4+} redox cycle [5]; Similarly, CuO also functions as the electron donor and acceptor, to maintain the Cu^{2+}/Cu^{3+} redox cycle [6]. For single metal site Co, they have demonstrated impressed activity, but suffer from sluggish kinetics of low-valence metal regeneration and poor durability [7]. To address these issues,

one common strategy is to build binary or polynary metal active site with synergistic interactions and different functionalities.

The synergistic effect between Co and Fe can significantly enhance the activity of Fenton-like reaction. Up to now, various crucial factors, including reducibility, surface-absorbed hydroxyl, adsorption-catalysis synergy, suppressed Co leaching by Fe, as well as electron transfer between Fe and Co, have been proposed to clarify the reason for Fe-Co synergy [8–14]. Thereinto, the role of surface-absorbed hydroxyl and electron transfer of Fe is still in debate [15]. Nevertheless, the fundamental mechanisms of Fe-Co synergy for enhancement in intrinsic activity of PMS activation are not fully understood yet.

Inspired by the molecule-level insight into the Fe-Mn synergy, the origin of catalytic activity and pathway lies in the catalyst surface electronic properties of Fe-O-Mn, which essentially accounts for the synergic catalysis [16]. Consequently, the obstacle to full understanding the intrinsic origin is the complexity in chemical composition and crystal structure [17–21]. Exactly, spinels, as an important class of TM oxide, are endowed with charming characteristics including controllable composition, structure, valence and morphology, as well as excellent

---

stability [22]. To better explore the synergy mechanism, in this work, the background contributions from coordination environment, valence state, and morphology are all ruled out by locating Co and Fe in the same geometrical site in spinels. Through this design strategy, the electronic structure-intrinsic activity-catalytic pathway relationship and Fe-Co synergy can be easily revealed.

We synthesized a series of Zn-Fe-Co spinel oxides with fixed tetrahedral (Td) sites by redox-inert Zn^{2+} and tuned catalytically critical octahedral (Oh) sites by Fe and Co with different ratios for PMS activation. By systematically investigating the electronic structure and corresponding catalytic behaviors, we identified TM_{oh}-O covalency as the decisive factor in determining the intrinsic catalytic activity of Zn-
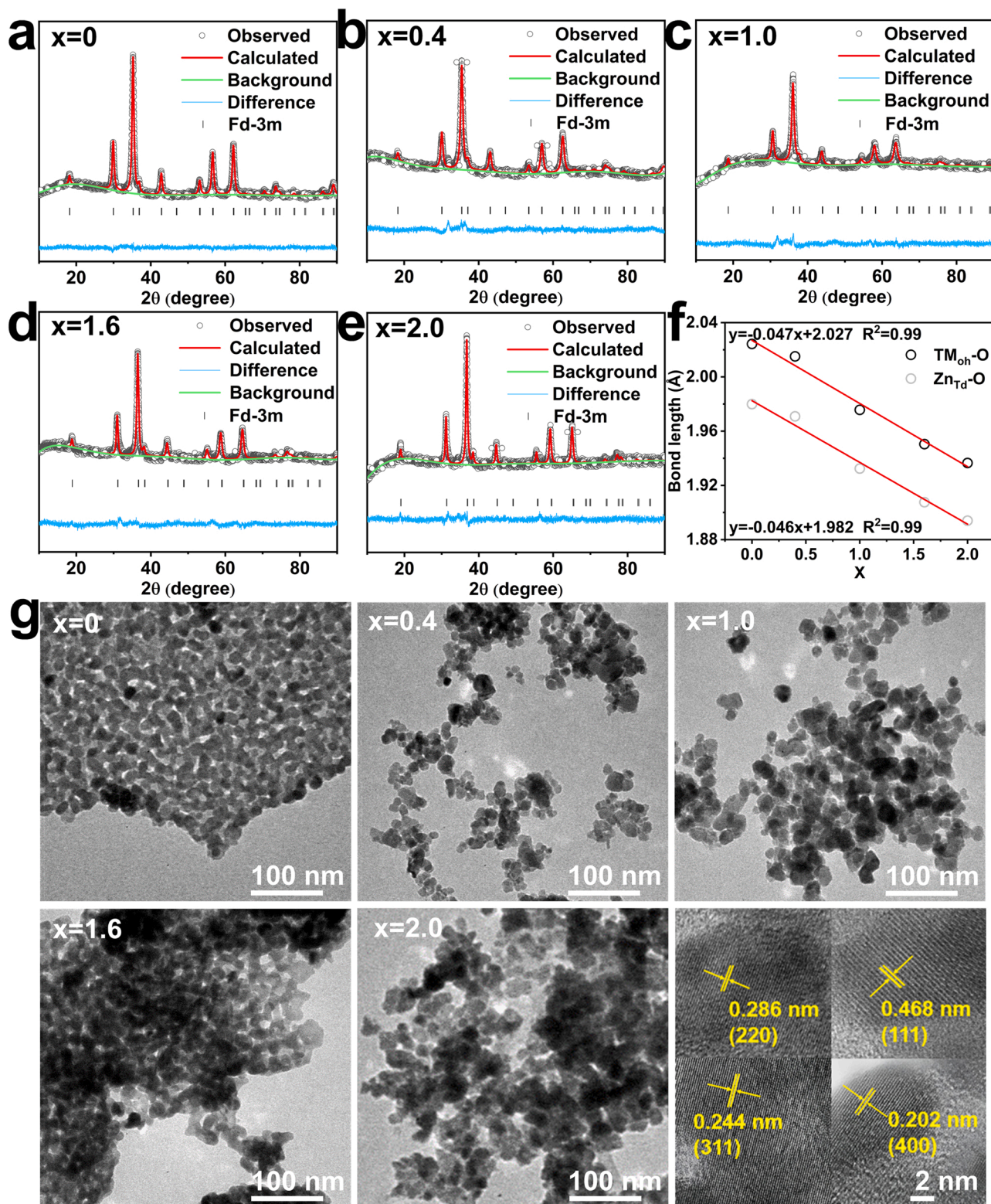

Fig. 1. Rietveld refinement results of as-synthesized $ZnFe_2O_4$ (a), $ZnCo_{0.4}Fe_{1.6}O_4$ (b), $ZnCoFeO_4$ (c), $ZnCo_{1.6}Fe_{0.4}O_4$ (d), and $ZnCo_2O_4$ (e). Evolution of the lattice parameter with the content of Co substitution (f); TEM images of $ZnCo_xFe_{2-x}O_4$ spinel oxides (x = 0–2.0) and HRTEM image of $ZnCo_{1.6}Fe_{0.4}O_4$ (g).

Fe-Co spinel oxides via both experimental analysis and theoretical calculation. Intriguingly, the mechanism of Fe-Co synergy in $(Co_{0.8}Fe_{0.2})_{Oh}$-O unit is deciphered by the favorable covalency competition. Specifically, the interplay between Co and Fe renders the $(Co_{0.8}Fe_{0.2})_{Oh}$-O unit a higher degree of electron delocalization at Co_{Oh} sites and lower degree of electron delocalization at Fe_{Oh} sites to enable highly efficient activation of PMS and suppressed generation of $^1O_2$ with less 2-chlorophenol (2-CP) reactivity. Finally, the high activity, stability, and environmental applicability of optimized catalysts for PMS activation and pollutant degradation are demonstrated.

2. Method

2.1. Chemicals

The detailed information of chemicals is provided in Text S1.

2.2. Synthesis and characterizations

Zn-Co-Fe spinel oxides were prepared with a sol-gel auto-combustion strategy. $Zn(OAc)_2 \cdot 2 H_2O$, $Co(OAc)_2 \cdot 4 H_2O$ and $Fe(NO_3)_3 \cdot 9 H_2O$ in specific molar ratio were dispersed in diluted HNO_3 (1 M, 32 mL), followed by the addition of 15 mmol citric acid with vigorous stirring. Then the mixture was maintained at 90 °C for 5 h to form viscous gel. After 170 °C thermal treatment for 12 h, the obtained product was grinded for 15 min and annealed in air at 400 °C for 6 h (ramping rate: 5 °C min^{-1}). The synthesis procedures for $ZnCo_2O_4$ and $ZnFe_2O_4$ are similar to those of Zn-Co-Fe spinel oxides except for the full replacement of Fe $(NO_3)_3 \cdot 9 H_2O$ by $Co(OAc)_2 \cdot 4 H_2O$ for the former and the full replacement of Co $(OAc)_2 \cdot 4 H_2O$ by $Fe(NO_3)_3 \cdot 9 H_2O$ for the latter.

Crystalline structures and bonding information were analyzed by an X-ray diffractometer, Raman spectroscopy and Fourier transform infrared (FTIR). Morphological images were obtained from a field emission scanning electron microscopy (FESEM) and transmission electron microscopy (TEM). The specific surface area and porosity were measured by a Micromeritics Gernimi VII analyzer. Electronic structures were investigated systematically by X-ray photoelectron spectroscopy (XPS) and X-ray absorption spectra (XAS). Co L-edge, Fe L edge, and O K-edge spectra were collected in the total electronic yield (TEY) mode at the BL08U1A beamline station of the Shanghai Synchrotron Radiation Facility (SSRF). Quantification for Co states was conducted via least squares fit of a linear combination of references to experimental data followed by integration of the respective curve areas. Co states present in the catalyst were simulated using Sr_2CoO_3Cl as a HS Co^{3+} reference with pyramidal coordination (taken from [23]), CoO as a HS Co^{2+} reference (taken from [24]), $SrCoO_3$ as a LS Co^{4+} reference (taken from [25]) and $LiCoO_2$ as a LS Co^{3+} reference in octahedral coordination. The cation content was measured by inductively coupled plasma-optical emission spectrometry (ICP-OES) and Energy Dispersive X-ray spectroscopy (EDX). The zeta potential of catalysts was tested using a zeta potential analyzer. The detailed information on instruments and techniques is listed in Table S1.

2.3. Experimental and analytical methods

All the catalytic oxidation experiments were conducted in a thermostatic mechanical stirring water bath. PMS stock solution (0.1 M, 0.5 mL) was injected into 2-CP solution (50 μM, 100 mL). The solution pH was controlled at the desired values by adding 0.1 M HCl or NaOH. After one minute to obtain homogeneity, 5 mg catalyst was added to trigger the catalytic oxidation reaction. At pre-determined time intervals, 500 μL of reaction solution was withdrawn, filtered and mixed with equal volume of $Na_2S_2O_3$. In recycling experiments, catalysts were recycled by filtration, cleaning, and oven-drying. Deactivated catalysts were regenerated by thermal treatment under 300 °C for three hours.

The concentration of pollutants, including 2-chlorophenol (2-CP),

phenol, atrazine (ATZ), bisphenol A (BPA), nitrobenzene (NB), and benzoic acid (BA), is analyzed by a high-performance liquid chromatography (HPLC) with a diode array detector. The degradation intermediates of 2-CP are identified by a HPLC-quadrupole time-of-flight mass spectrometry (Q-TOF-MS/MS). The existence and contribution of reactive oxygen species (ROS) for 2-CP degradation were revealed by quenching experiments and electron spin resonance (ESR) using 5,5-dimethyl-1-pyrrolidine-N-oxide (DMPO) and 2,2,6,6- tetramethylpiperidine (TEMP) as spin-trapping agents. In situ Raman and ATR-FTIR were conducted to investigate the interaction between catalysts and PMS. Detailed analysis procedures are provided in Text S2. CV curves and chronoamperometric measurements were employed to characterize the electron transfer capability. CV and amperometric i-t curves were measured by an electrochemical workstation in a standard three-electrode cell system with 0.1 M Na_2SO_4 as the electrolyte. The three-electrode cell was composed of a catalyst-loaded FTO glass working electrode, a platinum sheet counter electrode and a saturated Ag/AgCl reference electrode. For the preparation of the working electrode, catalysts were first dispersed in Nafion solution and then the catalyst ink (200 μL, 20 g/L) was drop-coated on the FTO glass (20 × 20 × 1.6 mm) for 3 times. The catalyst is dried in oven at 100 °C for 15 min. The response current of $ZnCo_xFe_{2-x}O_4$ (x = 0, 1.6, 2) after the addition of PMS (4 mM) and 2-CP (0.1 mM) was monitored with the chronoamperometry method.

2.4. Computational methodology

Density functional theory (DFT) calculations were carried out with the projector-augmented wave (PAW) method implemented in the Vienna Ab initio Simulation Package (VASP) [26,27]. The generalized gradient approximation (GGA) with the Perdew-Burke-Ernzerhof (PBE) functional was adopted to calculate the electron exchange and correlation energy. U_{eff} (U_{eff}=Coulomb U – exchange J) value is set to 4.0, 3.3, and 4.7 eV for Fe, Co, and Zn, respectively, proposed by Dudarev et al. [28,29]. The van der Waals interactions between layers were corrected by the DFT-D3 functional. The ions relaxation was achieved until the force for per atom was less than 0.02 eV/Å and the total energy converged to 10^{-5} eV. The theoretical models were constructed by a supercell (3 ×3 ×1). A 15 Å vacuum layer was constructed along the z-axis for each model to prevent interaction between adjacent slabs. The (400) surface was used to represent the catalytic surface.

3. Results and discussion

3.1. Physicochemical Properties

The diffraction patterns of as-synthesized samples match well with that of the standard face-centered cubic spinel structure with a Fd-3 m (227) space group (Fig. S1). XRD confirms the successful synthesis of spinel oxides, together with Raman spectrum (Fig. S2). Based on simulation results of Rietveld refinement, Zn is preferentially accommodated at Td sites, while Co and Fe cations occupy Oh sites (Fig. 1a-e, Table S2) [16]. With increasing Co substitution ratios, the bonds of Zn_{Td}-O and TM_{oh}-O shorten gradually, as evidenced by the high-angle shift of all diffraction peaks, and blue-shift of Zn_{Td}-O and TM_{oh}-O peaks in FTIR spectra (Fig. 1f and S3). The bond length change can be attributed to the fact that Co^{3+} has a smaller covalent radius (0.61 Å) than that of Fe^{3+} (0.65 Å), possibly affecting TM-O covalency [30]. For element composition analysis, the XPS general spectrum and EDS both confirm the existence of Zn, Co (for x = 0.4–2), Fe (for x = 0–1.6) and O (Figs. S4-S9). Elemental mappings confirm their homogeneous distribution (Figs. S10-S14). The ICP-OES analysis confirms that the calculated atomic ratios agree with stoichiometric ratios (Table S3). Apart from the variation in lattice parameter and Co/Fe content, $ZnCo_xFe_{2-x}O_4$ (x = 0–2.0) spinel oxides all exhibit similar morphological character, textural properties and polycrystalline nature without preferred crystallographic
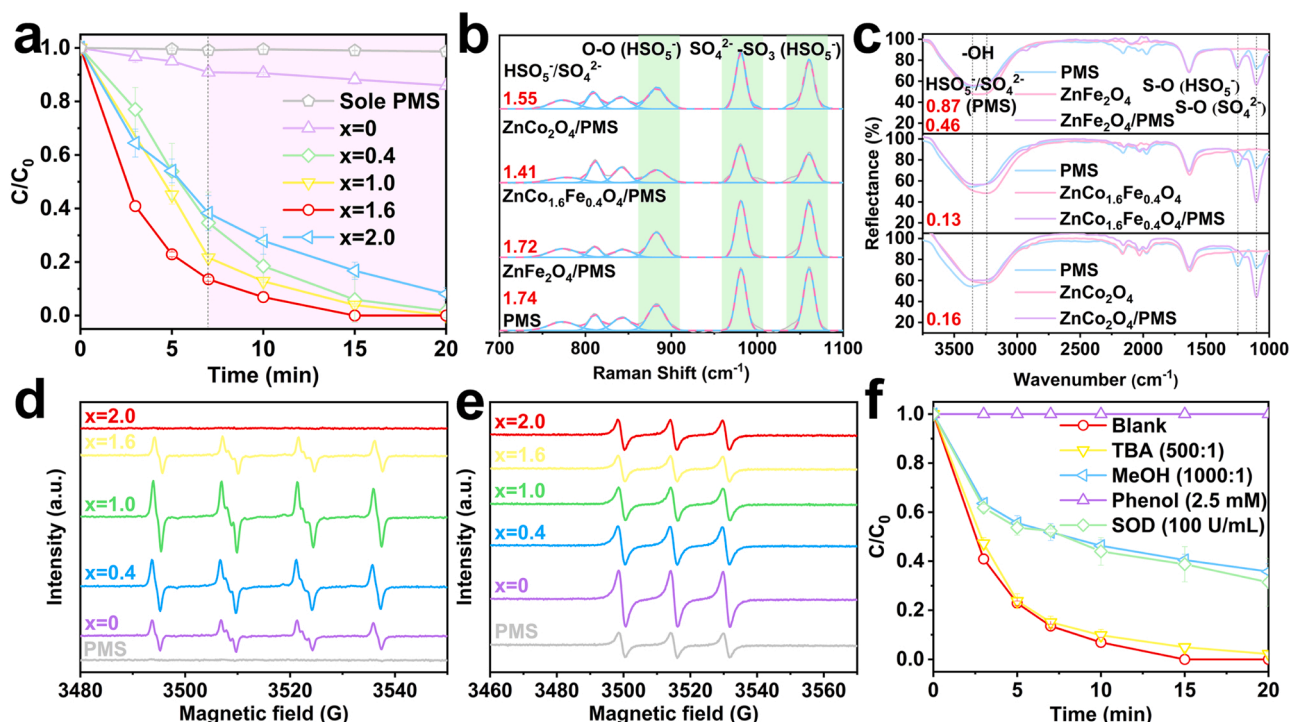
Fig. 2. . 2-CP removal performance of ZnCo$_x$Fe$_{2-x}$O$_4$ (x = 0–2.0) (a); In situ Raman spectra for PMS with/without the addition of ZnCo$_x$Fe$_{2-x}$O$_4$ (x = 0, 1.6, 2.0) (b); ATR-FTIR spectra for PMS solution, ZnCo$_x$Fe$_{2-x}$O$_4$ (x = 0, 1.6, 2) spinel oxides in water and in PMS solution (c); ESR spectra of the ZnCo$_x$Fe$_{2-x}$O$_4$ (x = 0–2.0)/PMS systems in solution using DMPO as a trapping agent (d); using TEMP as a trapping agent (e); Removal of 2-CP versus time in the ZnCo$_{1.6}$Fe$_{0.4}$O$_4$/PMS system with the addition of different quenchers. Conditions: pH = 7.0, [Catalyst] = 0.05 g/L, [PMS] = 0.5 mM, [2-CP] = 50 μM (f).

orientation (Fig. 1g, S15-S17, and Table S4). Specifically, the HRTEM image exhibits the interplanar spacing of 0.268, 0.468, 0.244, and 0.202 nm, which is assigned to the crystallographic plane (220), (111), (311), and (400) respectively.

3.2. Catalytic activity and pathway

The catalytic performances are evaluated using 2-CP as the model pollutant, due to its negligible adsorption on Fe and Co sites (Fig. S18). In Fig. 2a, ZnCo$_{1.6}$Fe$_{0.4}$O$_4$ shows the highest catalytic activity with re-action rate constant of 0.27 min^{-1}, which is 254.7, 37.5 and 2.2 times of that in sole PMS, ZnFe$_2$O$_4$/PMS system and ZnCo$_2$O$_4$/PMS system, respectively. The mineralization rate in 30 min is 0, 0.25%, 32.98%, 43.22%, 42.66% for ZnFe$_2$O$_4$/PMS, ZnCo$_{0.4}$Fe$_{1.6}$O$_4$/PMS, ZnCoFeO$_4$/PMS, ZnCo$_{1.6}$Fe$_{0.4}$O$_4$/PMS, and ZnCo$_2$O$_4$/PMS systems, respectively (Fig. S19). These results provide evidence for Fe-Co synergy. Addition-ally, the large activity disparity between ZnFe$_2$O$_4$ and ZnCo$_x$Fe$_{2-x}$O$_4$ (x = 0.4–2) substantiates that CoO$_6$ octahedra is the dominant catalytic unit, compared with FeO$_6$. To better reflect the intrinsic activity of catalysts, the reaction rate constant is calculated based on the kinetic data within 7 min (The rate-limiting factors become dominant after 7 min) and normalized to the SSA. Since the various ZnCo$_x$Fe$_{2-x}$O$_4$ (x = 0–2) tested in the experiments exhibit the similar SSA, the order of intrinsic activity is still consistent with that of the catalytic activity without normalization to SSA. Notably, ZnCo$_{1.6}$Fe$_{0.4}$O$_4$ outperforms all the previously reported Fe-Co based oxides in the activation of PMS and removal of refractory pollutants, with a modified rate constant as the index to offset the influence from reaction conditions including reactant concentration and catalyst dosage (Table S5).

The dynamic interactions between catalysts and PMS are investi-gated by in situ Raman and ATR-FTIR. PMS decomposition capability of a catalyst can be reflected by subtraction of the relative intensity of HSO$_5^-$ to SO$_4^{2-}$ for PMS from that for the catalyst/PMS. As shown in Fig. 2b and Table S6, PMS decomposition capability follows the order of

ZnFe$_2$O$_4$ < ZnCo$_2$O$_4$ < ZnCo$_{1.6}$Fe$_{0.4}$O$_4$. The same conclusion can also be drawn by analysis of ATR-FTIR (Fig. 2c, Table S7), further demon-strating the Fe-Co synergy in PMS activation. To be specific, obvious weakening and red-shifts of the S-O (HSO$_5^-$) stretching band are observed after the addition of ZnCo$_2$O$_4$ and ZnCo$_{1.6}$Fe$_{0.4}$O$_4$ into PMS, but no changes after the addition of ZnFe$_2$O$_4$. The red-shift indicates that active sites attract electron from the neighboring S-O bond, leaving it weaker (HSO$_5^- - e^- \rightarrow SO_5^{\bullet -} + H^+$). For aqueous slurries of catalysts, the broad band at 3240 cm^{-1} is attributed to stretching vibration of surface -OH [31]. After the addition of PMS, the surface -OH stretching band weakened and blue-shifted. The weakening of -OH band suggests HSO$_5^-$ bonds with the catalysts by replacing some surface -OH. The blue-shift of peak po-sition indicates the enhancement in the electron donating power of the bonded TM active site, arising from the lower valence state, and the oxidation of PMS. Altogether, the reduction of TM$_{Oh}$ and the oxidation of PMS are mainly involved in ZnCo$_x$Fe$_{2-x}$O$_4$ (x = 0, 1.6, 2)/PMS sys-tems. Co acts as the catalytically critical active site and exhibits much stronger interaction with PMS, and Fe substitution may induce a syn-ergistic effect with Co.

2-CP degradation intermediates in the ZnCo$_{1.6}$Fe$_{0.4}$O$_4$/PMS system were identified by the HPLC-Q-TOF-MS/MS, including maleic acid, 1,2,4-benzenetriol, 2-hydroxybenzaldehyde, acetic acid, and butane-dioic acid (Fig. S20). The degradation pathway is proposed in Fig. S21. 2-CP molecules are dechlorinated and hydroxylated to form 1,2,4-ben-zenetriol; 2-hydroxybenzaldehyde is produced by the combination of phenol and formyl radical. They could be further oxidized to benzo-quinone, which was then attacked to form low toxic butanedioic acid, maleic acid, and acetic acid via ring cleavage, and finally mineralized to CO$_2$ and H$_2$O.

To identify the ROS involved in the ZnCo$_x$Fe$_{2-x}$O$_4$ (x = 0–2)/PMS system, ESR characterizations were employed with DMPO and TEMP as trapping agents. In Fig. 2d, no signal was observed for PMS alone and ZnCo$_2$O$_4$/PMS system, while the signal of DMPO- O$_2^{\bullet -}$ was only observed for ZnCo$_x$Fe$_{2-x}$O$_4$ (x = 0–1.6)/PMS systems [32]. This is because Fe^{3+}
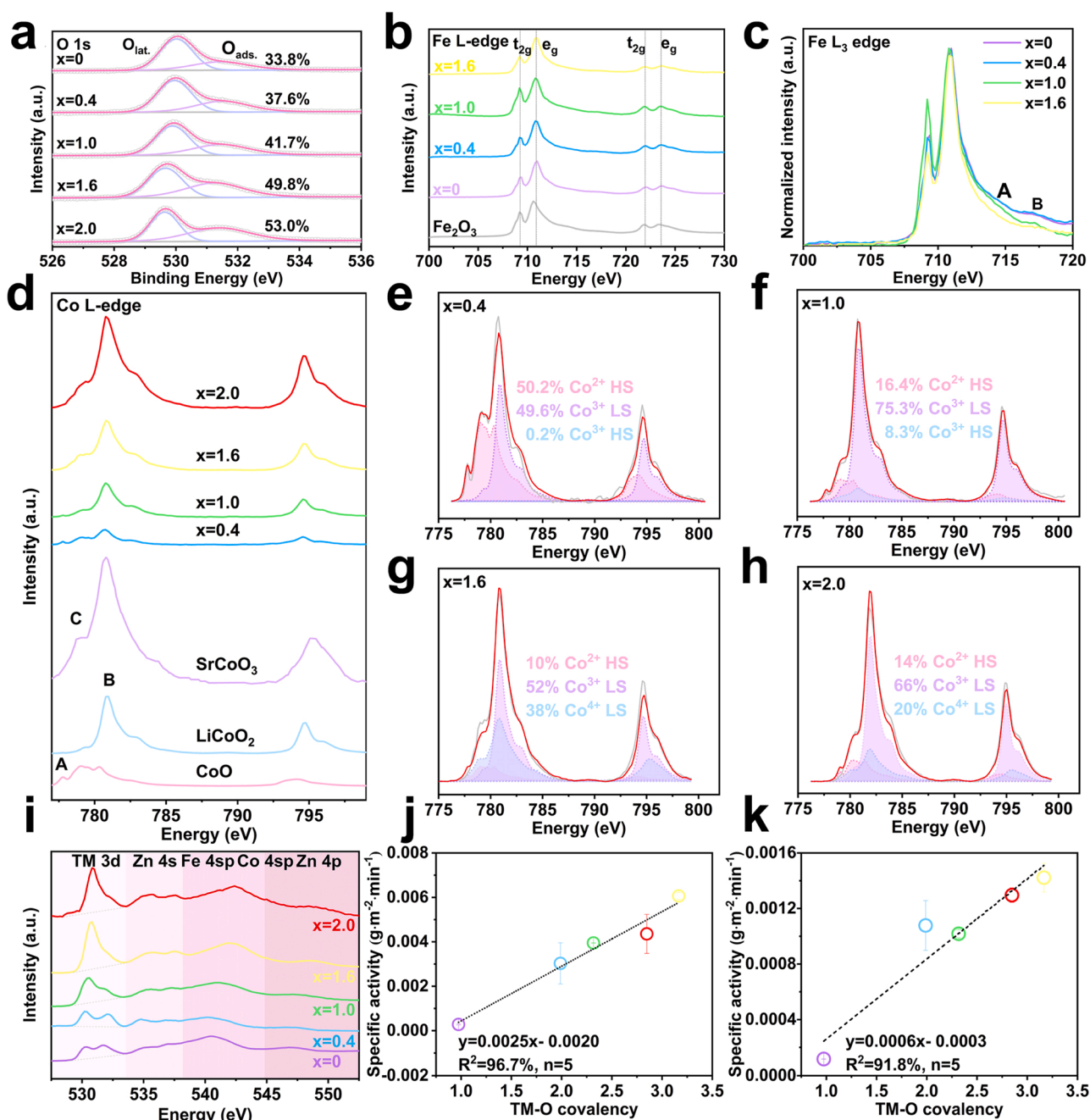
Fig. 3. O 1 s XPS (a); Fe $L_{3,2}$ XAS spectra (b); High resolution Fe L_3 XAS spectra (c); Co $L_{3,2}$ XAS spectra (d); Fitting of Co L-edge of $ZnCo_{0.4}Fe_{1.6}O_4$ (e), $ZnCoFeO_4$ (f), $ZnCo_{1.6}Fe_{0.4}O_4$ (g), and $ZnCo_2O_4$ (h); O K-edge XAS spectra and linear background subtraction of the pre-edge between the two nearest local minima (i); Correlation between TM-O covalency and intrinsic activity in PMS activation (j); Correlation between TM-O covalency and intrinsic 2-CP degradation rate (k).

can oxidize PMS primarily into $O_2^{\bullet-}$, which further evolves into $^1O_2$, and Co^{3+} oxidizes PMS into $SO_5^{\bullet-}$ with no detectable signals, which further evolves into $^1O_2$ and $SO_4^{\bullet-}$ [33,34]. For $ZnCo_{1.6}Fe_{0.4}O_4$/PMS system, the $SO_5^{\bullet-}$ concentration is high enough to produce amounts of $SO_4^{\bullet-}$. Since $^1O_2$ may also be generated from PMS self-decomposition, the signals of TEMP-$^1O_2$ adduct could be observed in all systems (Fig. 2e). We find the intensity of TEMP-$^1O_2$ and DMPO-$O_2^{\bullet-}$ individually shows negative (R^2 =96.7%) and no correlation (R^2 =0.1%) with the intrinsic activity, thus excluding the predominant contribution from $^1O_2$ and $O_2^{\bullet-}$ (Figs. S22 and S23). The negligible contribution of $^1O_2$ in 2-CP degradation is also demonstrated by the nonenhancement of degradation performance at higher pH (discussed in the Section 3.5), since the rate of singlet oxygenation of phenolic compounds increases with increasing pH, and PMS is also easily decomposed to $^1O_2$ under alkaline conditions [35].

In the representative $ZnCo_{1.6}Fe_{0.4}O_4$/PMS system, excessive methanol (MeOH), a common scavenger for $SO_4^{\bullet-}$ and ·OH inhibits the degradation of 2-CP from 100% to 60% in 15 min, while excessive TBA with more reactivity towards ·OH hardly inhibits the degradation of 2-CP (Fig. 2 f) [36]. The possibility of ·OH is also excluded due to the catalytic selectivity of the system for degradation of different refractory organics and low reactivity towards NB and BA, common ·OH probe compounds (Fig. S24). Furthermore, to confirm the existence and contribution of surface-bound $SO_4^{\bullet-}$ radicals, a stronger scavenger phenol was employed [37]. As expected, only 2.5 mM phenol inhibits the degradation of 2-CP completely. Besides $SO_4^{\bullet-}$, the contribution of $O_2^{\bullet-}$ to 2-CP degradation is also verified by the observed quenching effect of superoxide dismutase (SOD), which is inconsistent with the ESR results. This can be explained by the critical but indecisive role of $O_2^{\bullet-}$ in
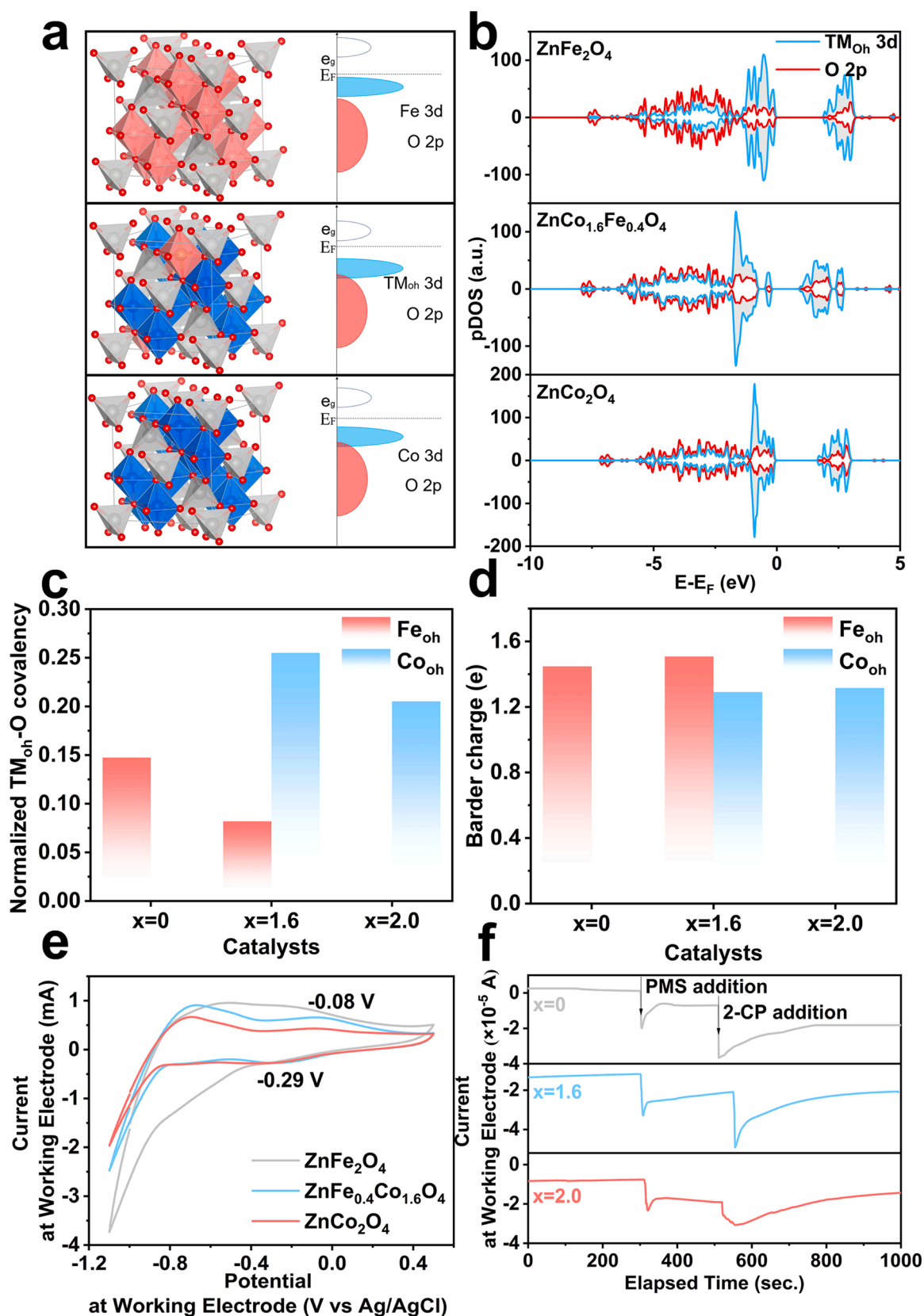
Fig. 4. Spinel structures and DFT calculated pDOS plots of the O 2p states and TM_{oh} 3d states (a), Schematic representation of the O p-band center (b), Normalized O 2p-TM_{oh} 3d hybridization percentage (c), Computed Barder charge of TM_{oh} (d), and CV curves of $ZnCo_xFe_{2-x}O_4$ (x = 0, 1.6, 2.0) (e); Chronoamperometric measurements upon addition of PMS and 2-CP using $ZnCo_xFe_{2-x}O_4$ (x = 0, 1.6, 2.0) nanoparticle-loaded FTO glass as working electrodes (f).

the regeneration of Co^{2+} [7]. Finally, the contribution of direct electron transfer is excluded as discussed in Section 3.4. Conclusively, the ESR and quenching experiments demonstrate that free and surface-bound $SO_4^{\bullet-}$ are the major contributors to pollutant degradation, while $O_2^{\bullet-}$ facilitates the generation of radicals with stronger oxidation ability.

3.3. Origin of intrinsic activity

To unravel the origin of intrinsic activity of $ZnCo_xFe_{2-x}O_4$ (x = 0–2.0), surface chemical composition and electronic properties of catalysts are explored by XPS and XAS. From O 1 s XPS (Fig. 3a), we find Co-rich catalysts possess stronger affinity with surface-absorbed oxygen species ($O_{ads.}$, ~531.4 eV), compared with Fe-rich ones, and the content of $O_{ads.}$ is linearly proportional to the Co content (R^2 =99%, Fig. S25). However, the intrinsic activity of the $ZnCo_xFe_{2-x}O_4$ catalysts is irrelevant to the content of Co (R^2 =54%) or O_{ads} (R^2 =70%) (Figs. S26 and S27). In high-resolution Zn 2p XPS (Fig. S28), two typical peaks of Zn 2p at 1044.5 eV and 1021.4 eV are ascribed to tetrahedral Zn^{2+}. Owing to its fully occupied d orbitals ($3d^{10}$) and redox-inert character, the catalytic contributions of itself, Zn_{Td}-O covalency or Zn_{Td}-O-TM_{Oh} super-exchange interaction are all excluded.

For Fe 2p XPS, the consistent peak position confirms that the valence state of Fe almost remains unchanged (Fig. S29). In Fe $L_{3,2}$ edge, both the spectral shape and energy position of main and shoulder peaks are the same for $ZnCo_xFe_{2-x}O_4$ (x = 0.4–2) and Fe_2O_3, indicating that Fe exists mainly in the form of HS Fe^{3+} ($t_{2g}^3 e_g^2$) (Fig. 3b). Features A and B in the high energy position are attributed to the charge transfer satellite, originating from Fe-O covalency (Fig. 3c) [38]. They become evident with increasing Fe substitution together with decreased intrinsic activity. In Fig. 3d, the sharp peak A at the lowest energy of the Co L_3-edge (777.8 eV) is characteristic of stable HS Co_{Oh}^{2+}. The Co_{Oh}^{2+} signal can be clearly observed in the spectra of $ZnCo_{0.4}Fe_{1.6}O_4$ and $ZnCoFeO_4$, while the multiplet spectral feature B of $LiCoO_2$ is found in all samples with varying spectral weight, indicative of different LS Co^{3+} content. The peak C at lower energy is ascribed to Co^{4+} ions, corresponding to the transition from the 2p state to one hole in the t_{2g} state [26]. Notably, the feature is present in the L_3-edge of $ZnCo_{1.6}Fe_{0.4}O_4$ spectrum. To accurately obtain the valence and spin state in $ZnCo_xFe_{2-x}O_4$ (x = 0.4–2), Co $L_{2,3}$-edges were analyzed quantitatively by a weighted superposition of the reference spectra of CoO as a HS Co_{oh}^{2+} reference, $LiCoO_2$ as a LS Co_{oh}^{3+} reference, Sr_2CoO_3Cl as a HS Co_{oh}^{3+} reference and $SrCoO_3$ as a LS Co_{oh}^{4+} reference (Fig. 3e-h and Table S8). Overall, the Co valence first increases from + 2.50 to + 3.28 with x from 0.4 to 1.6, then decreases to + 3.06 with x = 2.0. Since Co^{3+} and Co^{4+} ions exhibit similar XPS spectra and Co^{2+} can also be reflected by the satellite peak [9,39,40], we employ the ratio of sat./(Co^{2+} + Co^{3+}+ sat.) to provide clues to the valency variation, which decreases from x = 0.4–1.6 and then increases slightly (Fig. S30, Table S9). The trend coincides well with the results of XAS. It seems that Co valence is positively related with the intrinsic activity (Fig. S31). However, it makes no sense because Co^{2+} contributes to the direct generation of strong oxidizing radicals, compared with Co^{3+} [7]. Actually, for heterogeneous TM oxide catalysts, Co oxidation can reduce energy difference between Co 3d and O 2p and thus enlarge covalency, which may be the real reason [41]. Consequently, the discrepant catalytic activity is not decisively ascribed to the chemical composition or valence, but possibly to Co-O-Fe or Co/Fe-O covalency.

Raman spectra can give broad information on the bonding properties (Fig. S2). With raising Co content, Zn_{Td}-O stretching mode $F_{2g}^{(3)}$ shifts towards high wave-number, which denotes the strengthening and shortening of Zn_{Td}-O bond. Actually, the Zn_{Td}-O covalency (side-to-side orbital overlap) is far weaker than TM_{oh}-O covalency (head-on orbital overlap), and its subtle difference can be neglected, owing to the same charge deviation of Zn_{Td}, an indicator of Zn_{Td}-O covalency (Fig. S32). The blue-shift of TM_{oh}-O stretching mode A_{1g} with Co substitution from x = 0–1.6 arises from the strengthening of TM_{oh}-O bond. But from x = 1.6–2.0, the A_{1g} mode red-shifts obviously, denoting the weakening

of TM_{oh}-O bond, based on Hooke's law [42].

More detailed information on the bonding between TM 3d and O 2p is gained by analysis of O K-edge XAS spectra. In Fig. 3i, the first feature corresponds to the excitation from the O 1 s state to the hybridized O 2p-TM 3d state, the second, third, and fourth features originate in the excitations of O 1 s to O 2p-Zn 4s, O 2p-Fe/Co 4sp and O 2p-Zn 4p, respectively [43–45]. Thus, the first peak is employed to assess the degree of TM_{Oh} 3d - O 2p covalency (strong σ interaction), in view of negligible orbital overlap in tetrahedron (weak π interaction), negligible contribution of Zn_{Td}-O covalency to both TM-O covalency and intrinsic activity [46]. It is worth noting that the integrated area under the pre-peak requires normalization for abundance of unoccupied 3d states and different spectral contribution of e_g and t_{2g} holes. Specifically, holes in e_g states (he_g) contribute ~4 times more to the spectral intensity than those in t_{2g} states (ht_{2g}) [44,47]. Therefore, the TM_{Oh}-O covalency (x = 0–2.0) is determined by normalized intensity of O K prepeak to the sum of he_g and $1/4ht_{2g}$. Its value increases from x = 0–1.6 and decreases from x = 1.6 to x = 2.0. As shown in Figs. 3j and 3k, the high correlation between TM_{Oh}-O covalency and intrinsic activity is uncovered, from both aspects of 2-CP degradation (R^2 =96.7%) and PMS decomposition (R^2 =91.8%).

To directly reveal the degree of TM_{oh} -O covalency, DFT computation was carried out for $ZnFe_2O_4$, $ZnCo_{1.6}Fe_{0.4}O_4$, and $ZnCo_2O_4$ (Fig. 4a). The band centers for TM_{oh} 3d and O 2p are determined from the projected density of states (pDOS) (Fig. 4b). Their energy difference in $ZnFe_2O_4$ (1.99 eV) is obviously larger than that in $ZnCo_2O_4$ (1.29 eV) and $ZnCo_{1.6}Fe_{0.4}O_4$ (1.31 eV), indicating a stronger hybridization degree of TM_{oh}-O in $ZnCo_2O_4$ and $ZnCo_{1.6}Fe_{0.4}O_4$. As the determination method of band center also involves the energy states not involved in TM_{oh}-O bonding, a more accurate integration method is employed [46]. In Fig. 4c, the grey-colored area represents non-overlapped orbital between oxygen 2p and TM_{oh} 3d orbital, and the percentage of remaining overlapped area is a reflection of TM_{oh}-O covalency. A high correlation with R^2 coefficient of 99.1% is confirmed between the TM_{oh}-O covalency degree and intrinsic activity, further demonstrating the TM_{oh}-O covalency is a governor of the intrinsic activity (Fig. S33). Specifically, the degree of Co_{Oh}-O covalency is much higher than that of Fe_{Oh}-O covalency, indicative of the increased electron delocalization, electron conductivity and more critical catalytic role of Co_{Oh} over Fe_{Oh} sites (Fig. S34). The highest covalency degree is achieved by $ZnCo_{1.6}Fe_{0.4}O_4$, suggesting the synergy of Fe and Co.

Essentially, Fe/Co e_g orbitals participate in σ-bonding with PMS by overlapping with O 2p orbitals, thus its occupancy influences the bonding strength [48]. Based on the abundance of Co and Fe states obtained from XAS data in Figs. 2b-2h, the average e_g orbital occupancy level can be quantified. The relationship between e_g orbital occupancy and intrinsic catalytic activity is explored. As shown in Fig. S35, the intrinsic activity exhibits a volcano-shaped dependence on the e_g orbital occupancy of the TM 3d electron. The optimal e_g orbital occupancy is 0.55, with the highest TM_{oh}-O covalency. The catalytic kinetics and pathway can be well explained by simplifying the catalytic system, accurately studying the nature of electronic structure, establishing the quantitative structure-activity relationships (QSARs), and identifying the decisive activity descriptor.

3.4. Mechanisms of Fe-Co synergy

To decipher the mechanism of Fe-Co synergy, individual covalency degree of Co_{Oh}-O and Fe_{Oh}-O in $ZnCo_{1.6}Fe_{0.4}O_4$ is figured out and compared with that in $ZnCo_2O_4$ and $ZnFe_2O_4$, respectively, after normalization to their respective stoichiometry (Fig. S36). Clearly, the covalency between Co_{Oh} 3d and O 2p is enhanced from 0.205 to 0.255 by 20% Fe substitution, while that between Fe_{Oh} 3d and O 2p is weakened from 0.147 to 0.082 (Fig. 4d). The conclusion arrived from pDOS is consistent with that from the Barder charge analysis discussed as follows. Since the TM-O covalency originates from the polarization of
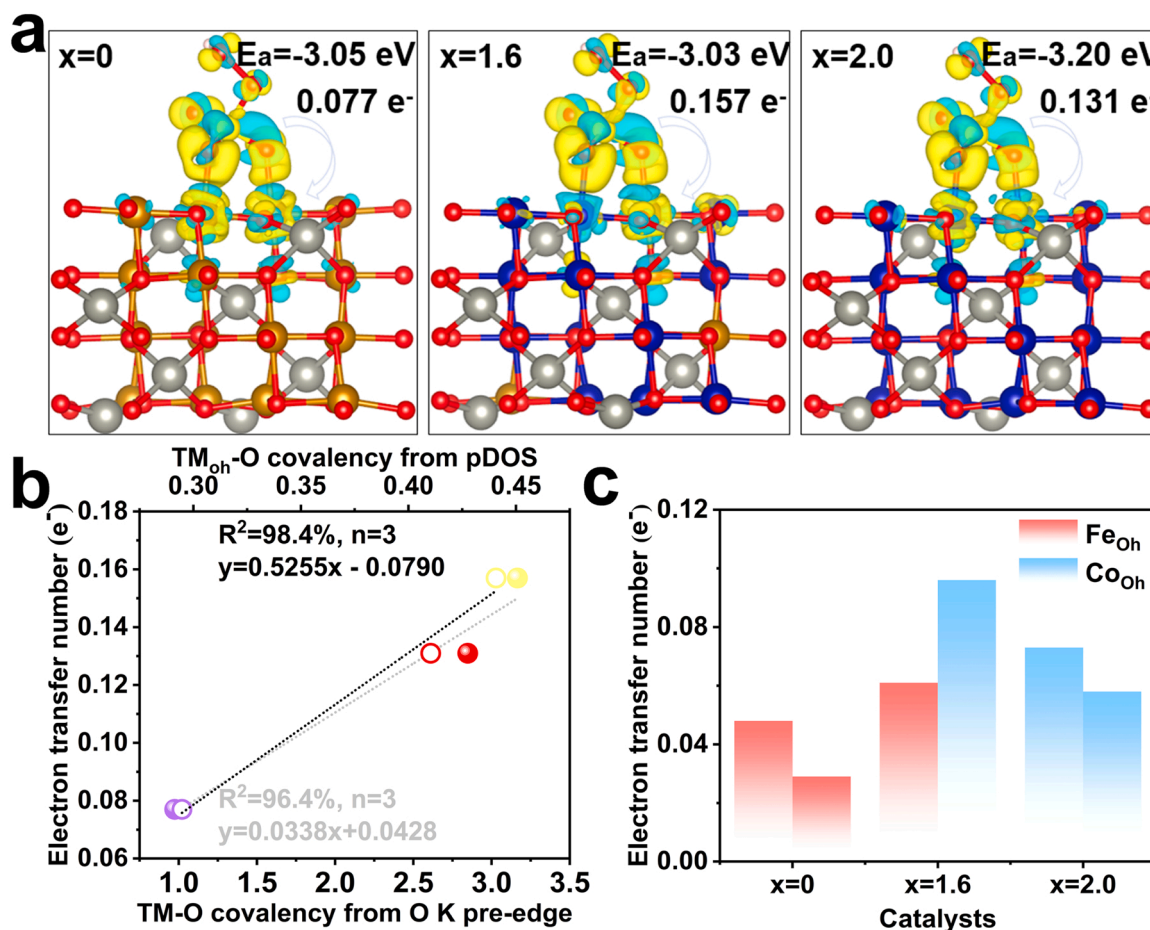
Fig. 5. Electronic transfer and PMS adsorption properties of $ZnCo_xFe_{2-x}O_4$ (x = 0, 1.6, 2.0) (a); Correlation between TM-O covalency between electron transfer number (b); Electron transfer numbers of active sites (c).

electrons from the O^{2-} anion into the TM cation or the sharing of electrons between O^{2-} anion and TM cation, the Co_{Oh}/Fe_{Oh} -O covalency can also be reflected by the deviation degree of calculated atomic charge from its formal ionic charge (nominal charge in ion-only systems, equal to +3 for Fe_{Oh}/Co_{Oh}) [49]. That is, higher deviation degree denotes greater sharing of electrons between O anions and TM cation, more covalent contribution in the TM-O bond and thus greater covalency. The calculated atomic charge is obtained by Barder charge analysis of electron density of each atom in $ZnCo_xFe_{2-x}O_4$. For the more covalent TM-O bond, the electron cloud shifts towards the interatomic region and delocalizes to a greater extent, accounting for smaller Barder charge. In the case of $ZnCo_{1.6}Fe_{0.4}O_4$, the calculated charge of Fe (+1.507) exhibits less deviation compared with $ZnFe_2O_4$ (+1.448), but that of Co (+1.290) exhibits greater deviation compared with $ZnCo_2O_4$ (+1.316), further confirming the enlarged Co_{Oh}-O covalency and weakened Fe_{Oh}-O covalency after Fe substitution (Fig. 4e). As such, we conclude that the oxygen charge tends to largely shift towards the catalytically critical Co_{Oh} sites rather than catalytically inert Fe_{Oh} sites, and gives stronger Co_{Oh}-O covalency and weaker Fe_{Oh}-O covalency, when O bonds covalently with Co_{Oh} and Fe_{Oh} [46]. Combined with the experimental evidence from O K XAS spectrum, it is found that although Fe substitution reduces Fe_{Oh}-O covalency, the loss is offset by enlarged Co_{Oh}-O covalency, which contributes more to total covalency character. Through this favorable covalency competition strategy optimizes the electron structure and promotes the intrinsic activity. Apart from increased occupation of catalytically critical Co_{Oh} site, the intrinsic activity can be also promoted by enhanced covalency degree.

To characterize the redox properties and explore its relationship with covalency, CV curves are recorded (Fig. 4f). $ZnCo_{1.6}Fe_{0.4}O_4$ and

$ZnCo_2O_4$ exhibit a pair of redox peaks at − 0.08 V/− 0.29 V, corresponding to the oxidation of Co^{3+} and reduction of Co^{4+}. $ZnCo_{1.6}Fe_{0.4}O_4$ exhibits smaller peak separation and higher redox current than those of $ZnCo_2O_4$, indicative of stronger redox reversibility of $ZnCo_{1.6}Fe_{0.4}O_4$. In contrast, almost no peak appears for $ZnFe_2O_4$. The above results demonstrates that electron transfer capability follows the order of $ZnCo_{1.6}Fe_{0.4}O_4 > ZnCo_2O_4 > ZnFe_2O_4$, consistent with the TM_{Oh}-O covalency and intrinsic activity. This suggests that TM_{Oh}-O covalency determines the intrinsic activity due to its positive role in electron polarization from O to TM_{Oh}, thus accelerating the electron transfer from oxygen-containing species PMS to active site TM_{Oh} and generation of the lower valence TM_{Oh}.

Chronoamperometry measurements are carried out to monitor the electron transfer process for the $ZnFe_2O_4$, $ZnCo_{1.6}Fe_{0.4}O_4$, and $ZnCo_2O_4$ samples as working electrodes, respectively (Fig. 4g). The injection of PMS at 300 s causes current jumps for the three spinel oxides, corresponding to the electron transfer between catalysts and PMS. Specifically, the current density decreased from − 1 to − 6.9 uA for $ZnFe_2O_4$, from − 1.2 to − 26 uA for $ZnCo_{1.6}Fe_{0.4}O_4$ and from − 7.6 to − 17 uA for $ZnCo_2O_4$. This demonstrates that the rate of electron transfer follows the order of $ZnCo_{1.6}Fe_{0.4}O_4 > ZnCo_2O_4 > ZnFe_2O_4$, which well agrees with the CV results. Thus, it can be concluded that catalysts with large TM_{Oh}-O covalency exhibit strong electron transfer capability and catalytic activity. The injection of 2-CP results in the same direction of current change, suggesting no electron transfer from target pollutant to the catalyst and thus exclusion of the direct electron transfer pathway as the possible degradation mechanism [49].

The specific electron transfer number from PMS to active sites is calculated by DFT. As shown in Fig. 5a, different catalyst models
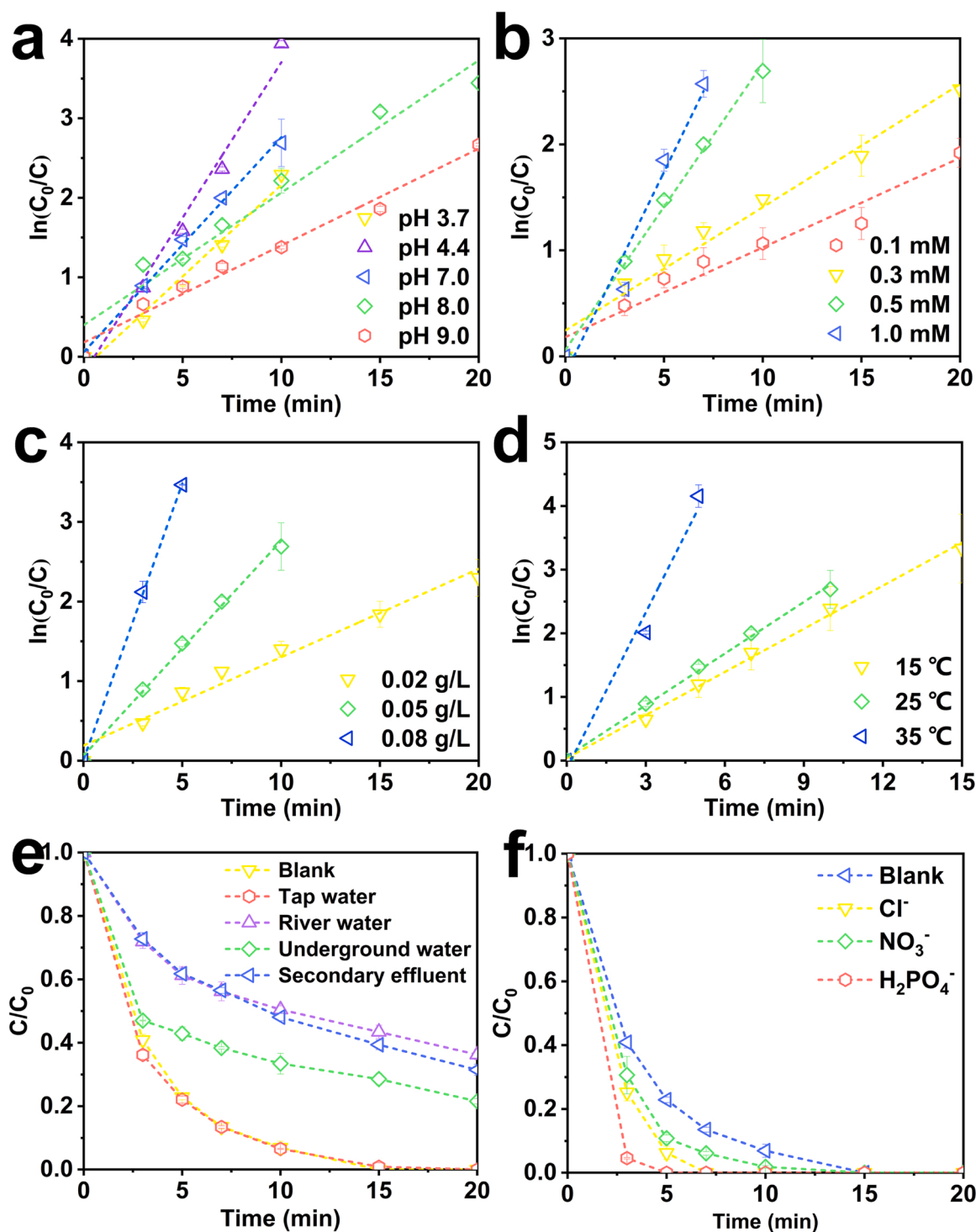
Fig. 6.. Effect of pH (a), PMS dosage (b), Catalyst dosage (c), Temperature (d); The degradation efficiency in different water matrices (e); The pseudo-first-order kinetic plot of $ZnCo_{1.6}Fe_{0.4}O_4$/PMS system for degradation of different pollutants (f).

$ZnCo_xFe_{2-x}O_4$ (x = 0, 1.6, 2) exhibit distinct electron transfer number but with similar adsorption energy (E_{ads}) ~3 eV. This indicates the TM-O covalency affects the intrinsic activity by PMS decomposition rather than PMS affinity. We also find the high correlation between electron transfer number and TM-O covalency calculated based on pDOS and O K pre-peak, respectively (Fig. 5b). This further confirms the important role of TM-O covalency in determining electron transfer capability and intrinsic activity and reveals the TM_{oh}-O covalency-electron transfer-intrinsic activity correlations. The synergy effect of Fe and Co is also

confirmed from the aspect of electron transfer capability (Fig. 5c). Apparently, the enhanced activity of Co arises from larger Co-O covalency and accelerated electron transfer, while the increased electron transfer number towards Fe_{Oh}^{3+} with lower Fe-O covalency is associated with increased Co_{Oh}^{2+} generation, resulting in Fe_{Oh}^{3+} reduction via Fe_{Oh}^{3+}-Co_{Oh}^{2+} superexchange interaction. Noteworthily, the Fe_{Oh}^{3+}-O-Co_{Oh}^{2+} superexchange interaction is much weaker as compared with the Co-O covalency, due to obvious increment in Co^{2+} content and slight increment in Fe^{3+} after PMS activation (Figs. S37, S38, and Table S10) [50].
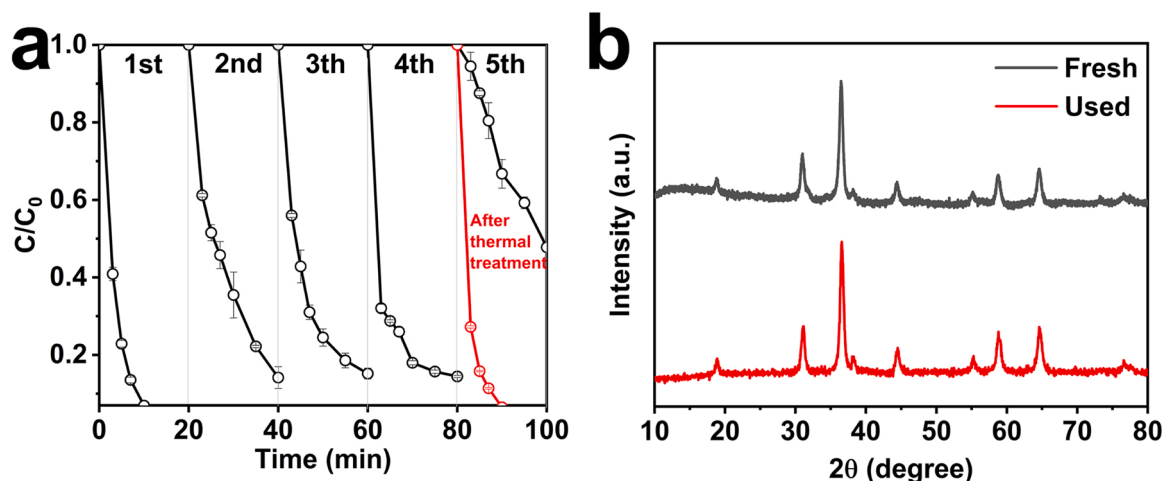
Fig. 7. The cycling runs in the $ZnCo_{1.6}Fe_{0.4}O_4$/PMS system for the degradation of 2-CP (a); XRD patterns for fresh and used $ZnCo_{1.6}Fe_{0.4}O_4$ (b).

Overall, the interplay between Co and Fe in $ZnCo_{1.6}Fe_{0.4}O_4$ can be explained by enlarged Co-O covalency and lowered Fe-O covalency, which accelerates the electron transfer between Co and O species to promote PMS activation and generation of free and surface-bound $SO_4^{\bullet-}$, as well as inhibits the electron transfer between Fe and O species to weaken the generation of $^1O_2$ with low 2-CP reactivity. Therefore, $ZnCo_{1.6}Fe_{0.4}O_4$ exhibits superior catalytic activity due to optimized electron structure.

3.5. Environmental applicability

The applicability of $ZnCo_{1.6}Fe_{0.4}O_4$/PMS system is assessed in different situations including the wide pH range from 3.7 to 9.0, reaction temperature and PMS dosage, the presence of coexisting ions, and the treatment of complex actual water (Fig. 6a-f). $ZnCo_{1.6}Fe_{0.4}O_4$ exhibits the highest activity at pH= 4.4, while the lowest activity at pH= 9.0. Since the isoelectronic point of catalyst is above 9 (Fig. S39), the possible reason for the low activity is attributed to the more deprotonated form of PMS (SO_5^{2-}) and generation of $^1O_2$ with low 2-CP reactivity under alkaline conditions. Overall, the $ZnCo_{1.6}Fe_{0.4}O_4$/PMS system shows a broad pH applicability. Increasing the catalyst dosage, PMS concentration, and reaction temperature can improve the catalytic efficiency. 2-CP can be completely degraded in 5 min with 0.08 g/L catalyst or at 35 °C. More importantly, higher reaction rate is also observed in the presence of $H_2PO_4^-$, Cl^- or NO_3^-. Cl^- can react with $SO_4^{\bullet-}$ radicals to produce reactive chlorine species ($Cl^\bullet$, $Cl_2^{\bullet-}$, HClO, and Cl_2) with different reactivity towards 2-CP [7]. In the presence of low level of Cl^-, $SO_4^{\bullet-}$ radicals are readily consumed to yield chlorine radicals ($Cl^\bullet$) [51]. $Cl^\bullet$ radicals are much more reactive towards benzene (6×10^9 $M^{-1}s^{-1} \leq$ $k(Cl^\bullet) \leq 1.2 \times 10^{10}$ $M^{-1}s^{-1}$) than $Cl_2^{\bullet-}$ radicals ($k_2 < 1 \times 10^5$ $M^{-1}s^{-1}$) and $SO_4^{\bullet-}$ ($k_3 = 3.0 \times 10^9$ M^{-1} s^{-1}) [52]. The presence of deactivating groups (inductive effect: $-NR_3 > -NO_2 > -COOH > -Cl > -OH$) on aromatic rings may decrease the reactivity of the $Cl^\bullet$ radical addition to the ring. With high dosage of Cl^-, $Cl_2^{\bullet-}/Cl_2$/HOCl become dominant active chlorine species, with poorer reactivity towards 2-CP. Conclusively, the type of dominant reactive chlorine species depends on the amount of Cl^- relative to $SO_4^{\bullet-}$. The promotion effect after addition of 5 mM Cl^- indicates that $Cl^\bullet$ with higher 2-CP reactivity dominants. The promotion effect of $H_2PO_4^-$ mainly comes from two aspects. It serves as the PMS activator to accelerate the generation of $SO_4^{\bullet-}$ [53]. Besides, it can strongly coordinate Fe_{Oh}^{3+} sites as a masking agent to inhibit the generation of $^1O_2$ with less 2-CP reactivity and increase the PMS utilization [54]. Unexpectedly, NO_3^- also exhibits positive effect, indicative of its Fe masking effect and optimized ROS type.

In different water matrices, the degradation of 2- CP is affected to different extent, compared with that in ultrapure water (Fig. 6e). Over 60% removal of 2-CP is still achieved in the treatment of actual water with complicated water chemistry, implying the potential of $ZnCo_{1.6}$-$Fe_{0.4}O_4$ for practical application. The type and concentration of dissolved organic carbon (DOC) and anions altogether exert combined effects on the degradation performance. To explore the individual effect, anion, turbidity, DOC and UV_{254} are measured. Based on the water quality analysis in Table S11, the inhibited performance in river water and secondary effluent is ascribed to high DOC, UV_{254}, and turbidity. By comparison of the performance in river water and secondary effluent, DOC is found as the main reason for the low removal efficiency, which serves as the reactive species competitor with target pollutant 2-CP. In addition, the relatively insignificant or positive effect from anion is demonstrated by the better performance in underground water with higher anion strength, compared with river water and secondary effluent. The anion anti-interference of $ZnCo_{1.6}Fe_{0.4}O_4$/PMS system originates from the important role of Fe masking effect and surface-bound reactive species [55].

The stability of $ZnCo_{1.6}Fe_{0.4}O_4$/PMS system is evaluated by the cyclic experiments. The degradation efficiency slightly decreases after the first cycle, then maintains till the fourth cycle, and dropped evidently at the fifth cycle. The catalyst after the fifth cycle can be fully recovered to original activity after thermal treatment (Fig. 7a). In addition, no change in crystal structure, morphology, and lattice oxygen is detected after catalytic oxidation reactions, and 83% Co and 99% Fe remains in catalysts (Fig. 7b, S40–42). Due to the high chemical stability, the declined activity is attributed to blockage of the active sites by degradation intermediates. Both high catalyst stability and catalytic activity originates from the strong chemical bonding between $(Co_{0.8}Fe_{0.2})_{Oh}$ cations and O anions.

4. Conclusions

In summary, we have studied the roles of Co_{oh}-O and Fe_{oh}-O covalency individually and together in activation of PMS and oxidation of 2-CP, by precluding the contribution of Td geometry. A high correlation between TM_{oh}-O covalency and intrinsic catalytic activity for PMS activation is found in Zn-Co-Fe spinel oxides, based on both experimental and theoretical investigation. The optimized $ZnCo_{1.6}Fe_{0.4}O_4$ shows the superior catalytic activity with reaction rate constant of 0.27 min^{-1}, which is 254.7, 37.5 and 2.2 times of that in sole PMS, Fe_{Oh}-O unit/PMS and Co_{Oh}-O unit/PMS systems, respectively. The mechanism of Fe-Co synergy for PMS activation is further deciphered by the favorable covalency competition, through comparative analysis of Fe_{Oh}-O, $(Co_{0.8}Fe_{0.2})_{Oh}$-O, and Co_{Oh}-O in terms of electronic structure,

catalytic properties, and electron transfer capability. Specifically, Co_{oh}^{3+} cations act as the catalytically critical active sites due to promoted Co_{oh}-O covalency, electron transfer capability and generation of $SO_4^{\bullet-}$. While Fe_{oh}^{3+} cations exhibit inert catalytic activity, but strengthen the Co_{oh}-O covalency at the cost of weakening the unfavorable Fe_{oh}-O covalency. Intriguingly, Fe-Co synergy strengthens the catalytic activity not only by optimizing the ROS type but also accelerating the electron transfer rate between catalysts and PMS. In addition to high intrinsic activity, the excellent stability, durability and environmental applicability of $ZnCo_{1.6}Fe_{0.4}O_4$ for PMS activation and pollutant degradation are also demonstrated.

CRediT authorship contribution statement

Wenqian Li: Conceptualization, Methodology, Formal analysis, Investigation, Data curation, Writing – original draft, Visualization. **Shuangqing Xia:** Data curation, Validation, Investigation. **Zhenyi Wang:** Data curation, Validation, Investigation. **Bin Zhang**: Data curation. **Boda Li**: Data curation. **Lijuan Zhang:** Data curation. **Kun Qian**: Data curation. Jun Ma: Resources, Supervision, Project administration, Funding acquisition. **Xu He:** Resources, Conceptualization, Writing – review & editing, Supervision, Project administration, Funding acquisition.

Declaration of Competing Interest

The authors declare that they have no known competing financial interests or personal relationships that could have appeared to influence the work reported in this paper.

Data Availability

Data will be made available on request.

Acknowledgments

Appendix A. Supporting information

Supplementary data associated with this article can be found in the online version at doi:10.1016/j.apcatb.2023.122358.

References

[1] B. Li, B. Ma, M. Wei, Y. Li, X. Fan, F. Zhang, G. Zhang, Q. Xia, W. Peng, Synthesis of Co-NC catalysts from spent lithium-ion batteries for fenton-like reaction: generation of singlet oxygen with~ 100% selectivity, Carbon 197 (2022) 76–86.

[2] M. Hervieu, A. Guesdon, J. Bourgeois, E. Elkaïm, M. Poienar, F. Damay, J. Rouquette, A. Maignan, C. Martin, Oxygen storage capacity and structural flexibility of $LuFe_2O_{4+x}$ ($0 \le x \le 0.5$), Nat. Mater. 13 (2014) 74–80.

[3] Z.Y. Guo, C.X. Li, M. Gao, X. Han, Y.J. Zhang, W.J. Zhang, W.W. Li, Mn- O covalency governs the intrinsic activity of Co-Mn spinel oxides for boosted peroxymonosulfate activation, Angew. Chem. Int. Ed. 60 (2021) 274–280.

[4] X. Wang, J. Li, K. Chen, J. Li, Y. Jia, Q. Mei, Q. Wang, Facile synthesis of oxygen vacancies enriched $ZnFe_2O_4$ for effective photocatalytic peroxodisulfate activation, Sep. Purif. Technol. 303 (2022), 122205.

[5] H. Li, N. Yuan, J. Qian, B. Pan, Mn_2O_3 as an electron shuttle between peroxymonosulfate and organic pollutants: The dominant role of surface reactive Mn (IV) species, Environ. Sci. Technol. 56 (2022) 4498–4506.

[6] Y. Wei, J. Miao, J. Ge, J. Lang, C. Yu, L. Zhang, P.J.J. Alvarez, M. Long, Ultrahigh peroxymonosulfate utilization efficiency over CuO nanosheets via heterogeneous Cu (III) formation and preferential electron transfer during degradation of phenols, Environ. Sci. Technol. 56 (2022) 8984–8992.

[7] W. Li, X. He, B. Li, B. Zhang, T. Liu, Y. Hu, J. Ma, Structural tuning of multishelled hollow microspheres for boosted peroxymonosulfate activation and selectivity: Role of surface superoxide radical, Appl. Catal. B-Environ. 305 (2022), 121019.

[8] Y. Ren, L. Lin, J. Ma, J. Yang, J. Feng, Z. Fan, Sulfate radicals induced from peroxymonosulfate by magnetic ferrospinel MFe_2O_4 (M= Co, Cu, Mn, and Zn) as heterogeneous catalysts in the water, Appl. Catal. B-Environ. 165 (2015) 572–578.

[9] L. Guo, L. Zhao, Y. Tang, J. Zhou, B. Shi, Peroxydisulfate activation using Fe, Co co-doped biochar and synergistic effects on tetracycline degradation, Chem. Eng. J. 452 (2023), 139381.

[10] W. Zhang, H. Zhang, X. Yan, M. Zhang, R. Luo, J. Qi, X. Sun, J. Shen, W. Han, L. Wang, J. Li, Controlled synthesis of bimetallic Prussian blue analogues to activate peroxymonosulfate for efficient bisphenol A degradation, J. Hazard. Mater. 387 (2022), 121701.

[11] S. Su, W. Guo, Y. Leng, C. Yi, Z. Ma, Heterogeneous activation of Oxone by $Co_xFe_{3-x}O_4$ nanocatalysts for degradation of rhodamine B, J. Hazard. Mater. 244 (2013) 736–742.

[12] P. Hu, M. Long, Cobalt-catalyzed sulfate radical-based advanced oxidation: a review on heterogeneous catalysts and applications, Appl. Catal. B-Environ. 181 (2016) 103–117.

[13] Q. Yang, H. Choi, S.R. Al-Abed, D.D. Dionysiou, Iron-cobalt mixed oxide nanocatalysts: heterogeneous peroxymonosulfate activation, cobalt leaching, and ferromagnetic properties for environmental applications, Appl. Catal. B Environ. 88 (2009) 462–469.

[14] J. Deng, M. Xu, S. Feng, C. Qiu, X. Li, J. Li, Iron-doped ordered mesoporous Co_3O_4 activation of peroxymonosulfate for ciprofloxacin degradation: performance, mechanism and degradation pathway, Sci. Total Environ. 658 (2019) 343–356.

[15] J. Zhao, H. Wei, P. Liu, A. Zhou, X. Lin, J. Zhai, Activation of peroxymonosulfate by metal-organic frameworks derived $Co_{1+x}Fe_{2-x}O_4$ for organic dyes degradation: a new insight into the synergy effect of Co and Fe, J. Environ. Chem. Eng. 9 (2021), 105412.

[16] Z.Y. Guo, Y. Si, W.Q. Xia, F. Wang, H.Q. Liu, C. Yang, W.J. Zhang, W.W. Li, Electron delocalization triggers nonradical Fenton-like catalysis over spinel oxides, Proc. Natl. Acad. Sci. USA 119 (2022), e2201607119.

[17] Y. Zhang, H. Liu, F. Gao, X. Tan, Y. Cai, B. Hu, Q. Huang, M. Fang, X. Wang, Application of MOFs and COFs for photocatalysis in CO_2 reduction, H_2 generation, and environmental treatment, EnergyChem 4 (2022), 100078.

[18] X. Liu, G. Verma, Z. Chen, B. Hu, Q. Huang, H. Yang, S. Ma, X. Wang, Metal-organic framework nanocrystal-derived hollow porous materials: Synthetic strategies and emerging applications, Innovation 3 (5) (2022), 100281.

[19] L. Wang, X. Ma, G. Huang, R. Lian, J. Huang, H. She, Q. Wang, Construction of ternary $CuO/CuFe_2O_4/g$-C_3N_4 composite and its enhanced photocatalytic degradation of tetracycline hydrochloride with persulfate under simulated sunlight, J. Environ. Sci. 112 (2022) 59–70.

[20] B. Su, H. Huang, Z. Ding, M.B.J. Roeffaers, S. Wang, J. Long, S-scheme $CoTiO_3$ /$Cd_{9.51}Zn_{0.49}S_{10}$ heterostructures for visible-light driven photocatalytic CO_2 reduction, J. Mater. Sci. Technol. 124 (2022) 164–170.

[21] L. Huang, B. Li, B. Su, Z. Xiong, C. Zhang, Y. Hou, Z. Ding, S. Wang, Fabrication of hierarchical $Co_3O_4@CdIn_2S_4$ p–n heterojunction photocatalysts for improved CO_2 reduction with visible light, J. Mater. Chem. A 8 (2020) 7177.

[22] Q. Zhao, Z. Yan, C. Chen, J. Chen, Spinels: controlled preparation, oxygen reduction/evolution reaction application, and beyond, Chem. Rev. 117 (2017) 10121–10211.

[23] Z. Hu, H. Wu, M.W. Haverkort, H.H. Hsieh, H.J. Lin, T. Lorenz, J. Baier, A. Reichl, I. Bonn, C. Felser, A. Tanaka, C.T. Chen, L.H. Tjeng, Different look at the spin state of ions in a pyramidal coordination, Phys. Rev. Lett. 92 (2004), 207402.

[24] J. Zhou, L. Zhang, Y. Huang, C. Dong, H. Lin, C. Chen, L.H. Tjeng, Z. Hu, Voltage- and time-dependent valence state transition in cobalt oxide catalysts during the oxygen evolution reaction, Nat. Commun. 11 (2020) 1984.

[25] S. Zhang, S. Gu, Y. Wang, C. Liang, Y. Yu, L. Han, S. Zheng, N. Zhang, X. Liu, J. Zhou, J. Li, Spontaneous delithiation under operando condition triggers formation of an amorphous active layer in spinel cobalt oxides electrocatalyst toward oxygen evolution, ACS Catal. 9 (2019) 7389–7397.

[26] P.E. Blöchl, Projector augmented-wave method, Phys. Rev. B 50 (1994) 17953–17979.

[27] G. Kresse, J. Furthmüller, Efficient iterative schemes for ab initio total-energy calculations using a plane-wave basis set, Phys. Rev. B 54 (1996) 11169–11186.

[28] S.L. Dudarev, G.A. Botton, S.Y. Savrasov, C.J. Humphreys, A.P. Sutton, Electron-energy-loss spectra and the structural stability of nickel oxide: an LSDA+ U study, Phys. Rev. B 57 (1998) 1505.

[29] G. Kresse, D. Joubert, From ultrasoft pseudopotentials to the projector augmented-wave method, Phys. Rev. B 59 (1999) 1758.

[30] G. Wu, J. Wang, W. Ding, Y. Nie, L. Li, X. Qi, S. Chen, Z. Wei, A strategy to promote the electrocatalytic activity of spinels for oxygen reduction by structure reversal, Angew. Chem. Int. Ed. 55 (2016) 1340–1344.

[31] Y. Shen, P. Wu, Two-dimensional ATR-FTIR spectroscopic investigation on water diffusion in polypropylene film: water bending vibration, J. Phys. Chem. B 107 (2003) 4224–4226.

[32] H. Gao, C. Huang, L. Mao, B. Shao, J. Shao, Z. Yan, M. Tang, B. Zhu, First direct and unequivocal electron spin resonance spin-trapping evidence for pH-dependent production of hydroxyl radicals from sulfate radicals, Environ. Sci. Technol. 54 (2020) 14046–14056.

[33] G.P. Anipsitakis, D.D. Dionysiou, Degradation of organic contaminants in water with sulfate radicals generated by the conjunction of peroxymonosulfate with cobalt, Environ. Sci. Technol. 37 (2003) 4790–4797.

[34] X. Bai, J. Shi, L. Xu, X. Jin, X. Shi, P. Jin, Fe-g-C_3N_4/reduced graphene oxide lightless application for efficient peroxymonosulfate activation and pollutant mineralization: comprehensive exploration of reactive sites, Sci. Total Environ. 855 (2023), 158799.

W. Li et al.

Applied Catalysis B: Environmental 325 (2023) 122358

[35] P.G. Tratnyek, J. Hoigne, Oxidation of substituted phenols in the environment: a QSAR analysis of rate constants for reaction with singlet oxygen, Environ. Sci. Technol. 25 (1991) 1596–1604.

[36] Z. Huang, H. Bao, Y. Yao, W. Lu, W. Chen, Novel green activation processes and mechanism of peroxymonosulfate based on supported cobalt phthalocyanine catalyst, Appl. Catal. B-Environ. 154 (2014) 36–43.

[37] H. Chen, Y. Xu, K. Zhu, H. Zhang, Understanding oxygen-deficient $La_2CuO_{4-\delta}$ perovskite activated peroxymonosulfate for bisphenol A degradation: the role of localized electron within oxygen vacancy, Appl. Catal. B-Environ. 284 (2021), 119732.

[38] D.Y. Kim, S. Miyoshi, T. Tsuchiya, S. Yamaguchi, Electronic defect formation in Fe-doped $BaZrO_3$ studied by X-ray absorption spectroscopy, Chem. Mater. 26 (2014) 927–934.

[39] Z. Lu, H. Wang, D. Kong, K. Yan, P.C. Hsu, G. Zheng, H. Yao, Z. Liang, X. Sun, Y. Cui, Electrochemical tuning of layered lithium transition metal oxides for improvement of oxygen evolution reaction, Nat. Commun. 5 (2014) 1–7.

[40] J. Wang, L. Li, J. Li, L. Meng, C. Xue, G. Li, Stabilizing Co^{4+} ions in ultrathin cobalt oxide nanosheets for efficient oxygen evolution reaction, ChemCatChem 10 (2018) 4888–4893.

[41] J. Suntivich, W.T. Hong, Y.L. Lee, J.M. Rondinelli, W. Yang, J.B. Goodenough, B. Dabrowski, J.W. Freeland, Y. Shao-Horn, Estimating hybridization of transition metal and oxygen states in perovskites from O K-edge X-ray absorption spectroscopy, J. Phys. Chem. C 118 (2014) 1856–1863.

[42] C. Shan, Y. Zhang, Q. Zhao, K. Fu, Y. Zheng, R. Han, C. Liu, N. Ji, W. Wang, Q. Liu, Acid etching-induced in situ growth of λ-MnO_2 over CoMn spinel for low-temperature volatile organic compound oxidation, Environ. Sci. Technol. 56 (2022) 10381–10390.

[43] M. Ghiasi, M.U.D. Jaime, A. Malekzadeh, R. Wang, P.S. Miedema, M. Beye, F.M. F. Groot, Mn and Co charge and spin evolutions in $LaMn_{1-x}Co_xO_3$ nanoparticles, J. Phys. Chem. C 120 (2016) 8167–8174.

[44] J. Simböck, M. Ghiasi, S. Schönebaum, U. Simon, F.M.F. Groot, R. Palkovits, Electronic parameters in cobalt-based perovskite-type oxides as descriptors for chemocatalytic reactions, Nat. Commun. 11 (2020) 1–10.

[45] X. Huang, J. Zhang, M. Wu, S. Zhang, H. Xiao, W. Han, T.L. Lee, A. Tadich, D.C. Qi, L. Qiao, L. Chen, K. Zhang, Electronic structure and p-type conduction mechanism of spinel cobaltite oxide thin films, Phys. Rev. B 100 (2019), 115301.

[46] S. Sun, Y. Sun, Y. Zhou, S. Xi, X. Ren, B. Huang, H. Liao, P.L. Wang, Y. Du, Z.J. Xu, Shifting oxygen charge towards octahedral metal: a way to promote water oxidation on cobalt spinel oxides, Angew. Chem. 131 (2019) 6103–6108.

[47] J. Suntivich, W.T. Hong, Y.L. Lee, J.M. Rondinelli, W. Yang, J.B. Goodenough, B. Dabrowski, J.W. Freeland, Y. Shao-Horn, Estimating hybridization of transition metal and oxygen states in perovskites from O K-edge X-ray absorption spectroscopy, J. Phys. Chem. C 118 (2014) 1856–1863.

[48] J. Miao, Y. Zhu, J. Lang, J. Zhang, S. Cheng, B. Zhou, L. Zhang, P.J.J. Alvarez, M. Long, Spin-state-dependent peroxymonosulfate activation of single-atom M–N moieties via a radical-free pathway, ACS Catal. 11 (2021) 9569–9577.

[49] X. Zhou, M.K. Ke, G.X. Huang, C. Chen, W. Chen, K. Liang, Y. Qu, J. Yang, Y. Wang, F. Li, H.Q. Yu, Y. Wu, Identification of Fenton-like active Cu sites by heteroatom modulation of electronic density, Proc. Natl. Acad. Sci. USA 119 (2022), e2119492119.

[50] T. Yamashita, P. Hayes, Analysis of XPS spectra of Fe^{2+} and Fe^{3+} ions in oxide materials, Appl. Surf. Sci. 254 (2008) 2441–2449.

[51] D.O. Martire, J.A. Rosso, S. Bertolotti, G.C.L. Roux, A.M. Braun, M.C. Gonzalez, Kinetic study of the reactions of chlorine atoms and $Cl_2^{\bullet-}$ radical anions in aqueous solutions. II. Toluene, benzoic acid, and chlorobenzene, J. Phys. Chem. A 105 (2001) 5385–5392.

[52] M.L. Alegre, M. Gerones, J.A. Rosso, S.G. Bertolotti, A.M. Braun, D.O. Martire, M. C. Gonzalez, Kinetic study of the reactions of chlorine atoms and $Cl_2^{\bullet-}$ radical anions in aqueous solutions. I. Reaction with benzene, J. Phys. Chem. A 104 (2000) 3117–3125.

[53] P. Duan, X. Liu, B.M. Liu, Y. Li, J. Pan, Q. Yue, B. Gao, X. Xu, Effect of phosphate on peroxymonosulfate activation: Accelerating generation of sulfate radical and underlying mechanism, Appl. Catal. B- Environ. 298 (2021), 120532.

[54] H. Ming, P. Zhan, Y. Yang, Y. Zou, C. Yang, Y. Hou, K. Ding, J. Zhang, X. Wang, Tailored poly-heptazine units in carbon nitride for activating peroxymonosulfate to degrade organic contaminants with visible light, Appl. Catal. B-Environ. 311 (2022), 121341.

[55] S. Wang, L. Xu, J. Wang, Iron-based dual active site-mediated peroxymonosulfate activation for the degradation of emerging organic pollutants, Environ. Sci. Technol. 55 (2021) 15412–15422.